An *in silico* investigation into polyester adsorption onto alumina towards an improved understanding of hydrogenolysis catalysts

---

Ziyue Dong[1], Erin E. Dunphy[1], Aidan B. Wegner[1], J. Will Medlin[1], Michael F. Toney[1,2,3], Kayla G. Sprenger[1]**

[1]Department of Chemical & Biological Engineering, University of Colorado Boulder,
Boulder, Colorado 80309, United States

[2]Materials Science & Engineering Program, University of Colorado,
Boulder, Colorado 80309, United States

[3]Renewable & Sustainable Energy Institute, University of Colorado,
Boulder, Colorado 80309, United States

Ziyue Dong (ziyue.dong@colorado.edu) https://orcid.org/0000-0001-8332-9212
J. Will Medlin (will.medlin@colorado.edu) https://orcid.org/0000-0003-2404-2443
Michael F. Toney (michael.toney@colorado.edu) https://orcid.org/0000-0002-7505-7920
Kayla G. Sprenger (kayla.sprenger@colorado.edu) https://orcid.org/0000-0002-7513-1166

Abstract

Chemical recycling of end-of-life plastic wastes through hydrogenolysis is a promising pathway for achieving a circular plastics economy and reducing overall energy costs. Understanding molecular interactions at the inorganic-organic depolymerization interface is crucial for enhancing catalyst performance and overcoming challenges posed by mixed plastic waste streams. We investigated a fundamental step in the depolymerization process: physisorption of polymers onto the metal oxide support preceding diffusion to and reaction at the catalyst-support junction. Molecular dynamics simulations, augmented with well-tempered metadynamics, were conducted to explore the adsorption of polylactic acid (PLA) and polyethylene terephthalate (PET) oligomers onto a hydroxylated alumina support surface. Our findings revealed multiple layers of highly oriented solvent molecules (1,4-dioxane) above the surface, creating significant barriers to polyester adsorption. Disrupting and displacing these solvent layers led PET oligomers to adsorb closer to and interact stronger with the surface than PLA oligomers, possibly contributing to the higher reaction temperatures needed to achieve full conversion in PET versus PLA hydrogenolysis. We further suggest an experimental approach to validate our results of solvent layering behavior through predictions of X-ray reflectivity that are consistent with our initial experiments. The insights gained in this study can be leveraged to refine our understanding of catalytic mechanisms to predict depolymerization reactivity and selectivity and improve future hydrogenolysis catalyst designs.

Introduction

Discovering alternative processing routes for end-of-life plastics is critical in advancing towards a circular plastics economy and developing sustainable, carbon-neutral energy infrastructure[1–4]. Currently, a significant portion of plastic waste ends up in landfills or is incinerated for energy recovery[1,2], primarily due to challenges associated with existing recycling processes. For instance, mechanical recycling of thermoplastics presents economic challenges, as these materials are expensive to physically sort due to the presence of various contaminants and additives[3]. Contaminants also limit the applications of recycled thermoplastics, particularly in areas such as food packaging, where stringent regulations impede closed-loop recycling[2,5]. Additionally, recycled thermoplastics often suffer from compromised mechanical properties and diminished quality, resulting in downcycled materials[1]. These considerations point to the importance of advancing polymer recycling in implementing the energy transition.

"Upcycling" polymers through chemical processing is a sustainable strategy for generating new, value-added chemical products from existing plastic waste streams. Through selective breakdown to their base monomers[1,6,7] or direct chain functionalization[8], these processes provide alternative routes for chemically transforming end-of-life plastic waste. By repurposing plastic waste as new polymers or as other products such as fuels, chemical recycling offers environmental and economic incentives for depolymerization. Moreover, chemical recycling processes have the potential to be highly effective at handling mixed and contaminated plastic waste that cannot be subjected to thermomechanical recycling, resulting in reduced processing complexities and costs[4].

Chemical recycling of end-of-life polymers through hydrogenolysis (cleavage of carbon-carbon or carbon-oxygen single bonds by hydrogen addition) with supported-metal catalysts enables the synthesis of value-added chemical products, showing promising selectivity for polyesters and polyolefins[5–12]. However, unlocking the full potential of this process hinges on a comprehensive understanding of polymer-catalyst interactions at the molecular level. Direct characterization of the polymer-catalyst interface, through both computational and experimental approaches, is essential for elucidating the conformations and interactions of adsorbed polymers. This knowledge can then be leveraged to guide the design of more effective hydrogenolysis catalysts.

The interaction of polymers with metal oxide surfaces is crucial for various catalytic processes. In supported-metal catalysts for hydrogenolysis, for example, the support material provides a structural framework to stabilize metal catalysts. Highly porous metal oxide supports such as alumina (Al_2O_3), silica (SiO_2), and titania (TiO_2) not only enable additional surface area for the dispersion of active metal nanoparticles but also enhance the mechanical robustness of the catalyst[13,14]. These supports play an important role in determining the number of active sites and their surrounding electronic environment through metal–support interactions, which are significant for overall catalytic performance[14,15]. Furthermore, the support itself can be kinetically active and thus influence catalyst activity, especially in the case of single-atom catalysts[16,17]. Modifications to the support (e.g., via acid-site concentration tuning or addition of self-assembled monolayers) can also directly impact reaction kinetics[15,18,19], highlighting the importance of support-polymer interactions. Beyond hydrogenolysis, metal oxide supports are used in other polymer-related catalytic processes, such as aluminosilicate zeolites in pyrolysis for polymer degradation[20]. Despite their broad applications, a detailed understanding of the molecular interactions between metal oxide support surfaces and polymers, including polyesters, is still lacking.

Supported ruthenium (Ru)-based catalysts have shown high effectiveness in selectively breaking down polyesters and polycarbonates into various diol products[1,4,5]. This class of catalysts has also exhibited remarkable efficacy in depolymerizing polyolefins like polyethylene and polypropylene. These catalysts convert long-chained hydrocarbons into alkanes with high liquid product conversion via metal surface C-C bond cleavage, aided by metal-support interactions[6,9–12]. Thus, hydrogenolysis with Ru-based catalysts presents an innovative yet practical approach to chemical recycling of end-of-life polymers, paving the way towards a sustainable circular plastics economy.

As mentioned earlier, there are currently knowledge gaps in our understanding of how polymers interact with metal oxide surfaces at the molecular level. While experimental methods such as adsorption isotherms are common in the field, they are challenging to implement with polymers due to their complex behavior. Single-molecule microscopy methods, such as fluorescence correlation spectroscopy (FCS), fluorescence recovery after photobleaching (FRAP), and single-molecule fluorescence resonance energy transfer (SM-FRET), have proven successful in describing the adsorption behavior of single molecules onto surfaces and guiding strategies for controlling adsorption strength and behavior[21–24]. These methods are particularly important because they offer high sensitivity and specificity, allowing for detailed insights into adsorption dynamics and molecular interactions that are difficult to capture with bulk techniques.

Nonetheless, existing experimental imaging techniques typically lack the necessary time and spatial resolution to capture atomic-level details. This provides a unique opportunity to synergistically combine computational approaches such as molecular dynamics (MD) simulations with experimental interfacial characterization techniques like fluorescence methods as well as X-ray scattering to achieve complementary insights into polymer physisorption. Moreover, employing enhanced sampling methods such as metadynamics[25–28] can improve the accuracy of MD simulations of solid-liquid interfaces. These techniques help accelerate sampling within the simulation to overcome strong binding forces that exist at the interface, ensuring comprehensive sampling of the conformational ensemble of physisorbed polymer states and facilitating better comparisons against experimental data.

Previous MD simulations of the adsorption behavior of polymers on metal oxide surfaces have primarily focused on bulk polymers in the form of solvated polymer chains and polymer melts to study their chain dynamics at the solid-liquid interface[29–31]. Yet, these studies have been limited to characterizing the physical dynamics of bulk polymer chains near the surface, which rely heavily on polymer-polymer interactions. Consequently, they do not fully capture the conformational dynamics of individual surface-bound polymers, that are influenced by isolated polymer-surface and solvent-surface interactions during adsorption and desorption. A recent study by Tong et al. successfully modeled the interface of several polymer inhibitors (PAA: poly(acrylic acid); PAM: poly(acrylamide); and PEG: poly(ethylene glycol)) adsorbing onto β-dicalcium silicate (C_2S), providing meaningful descriptions of polymer-surface and solvent-surface interactions[32]. However, this study did not offer insights into the impacts of surface-bound hydrogens, which are common in metal oxide supports of hydrogenolysis catalysts, on polymer-surface interactions.

In this study, we characterized the interfacial interactions between polyester oligomers, specifically polylactic acid (PLA) and polyethylene terephthalate (PET), and a hydroxylated alumina support surface during surface adsorption and desorption processes. Polylactic acid (PLA), a polyester composed of lactic acid joined by ester linkages, is widely recognized as one of the most utilized synthetic and biodegradable polymers[4,33]. Polyethylene terephthalate (PET), the most widely used polyester, is composed of terephthalic acid and ethylene glycol joined by ester linkages and has garnered significant attention as the most studied synthetic polymer for catalytic depolymerization[3,5]. During hydrogenolysis, PLA typically breaks down into 1,2-propanediol, while PET breaks down into ethylene glycol and 1,4-benzene dimethanol[4,5]. Notably, Westhues et al. reported drastically higher reaction temperature requirements for achieving full conversion in PET hydrogenolysis compared to PLA when using Ru catalysts in a 1,4-dioxane solvent environment[5]. This finding provides a route towards mixed stream polyester processing through temperature and solubility tuning. Yet, the factors controlling rate trends in polyester depolymerization on solid catalysts remain poorly understood. Molecular-level insights into optimizing catalyst designs can significantly improve the viability of hydrogenolysis and other catalytic processes for the chemical recycling of end-of-life plastic wastes. Successful implementation of such strategies will decrease the need for producing virgin plastics, which entails high energy costs and substantial carbon emissions. Chemical recycling of existing plastic waste streams through improved hydrogenolysis can facilitate the transition towards a more sustainable energy infrastructure by reducing the carbon footprint of plastics consumption.

In Ru-catalyzed hydrogenolysis, the thermodynamics of polymer adsorption and subsequent transport to the active site may be significantly influenced by polymer-support interactions, given the typically higher surface area of metal oxide supports compared to dispersed metal nanoparticles and especially single atoms[6,14]. Thus, our objective in this study was to utilize MD simulations to uncover the thermodynamic interactions occurring at the solvent-support interface during polymer surface adsorption and desorption. This approach enabled a fundamental study of the role of polymer physisorption thermodynamics during hydrogenolysis without the added complexity of Ru nanoparticles. Specifically, we focused on the interactions between polyesters oligomers (PLA and PET) and a hydroxylated alumina surface, a model for materials widely used as catalysts and catalyst supports. To our knowledge, this study represents the first application of long-timescale MD, augmented by enhanced sampling techniques, to investigate single-polymer adsorption behavior at a metal oxide/solvent interface. The workflow developed in this study can be applied to elucidate interfacial interactions in other important inorganic-organic systems, such as those involving electrolyte molecules and electrode surfaces in lithium-ion batteries[58-60].

Methods

Parameterization of polymer and solvent molecules

Structures of polyesters, polylactic acid (PLA) and polyethylene terephthalate (PET), along with the solvent 1,4-dioxane, were constructed using Avogadro[34]. Oligomeric models for PLA pentamer and decamer (PLA5 and PLA10, respectively) and PET dimer and trimer (PET2 and PET3, respectively), were built based on their respective number of repeated monomer units (**Table 1**). The end-to-end distances of these oligomers were determined to be 1.8 nm for PLA5, 2.2 nm for PET2, 3.5 nm for PLA10, and 3.4 nm for PET3. Next, all polymer and solvent molecules underwent parameterization using the electronic structure program Gaussian[35], with calculations conducted at the Hartree-Fock (HF) level of theory with the 6-31G* basis set. Of note, the selection of longer polyester chain lengths (PLA10 and PET3) was limited by the maximum number of atoms that can be accurately parameterized in Gaussian. Atomic point charges were assigned via Antechamber[36] with the RESP[37] method. Subsequently, the topologies for these molecules were generated with tLEaP[38] using parameters from the General Amber Force Field 2 (GAFF2[39]). Finally, the topologies were converted from AMBER to GROMACS format using ACPYPE[40].

Surface construction and parameterization

The structure of alumina, representing the hydroxylated (0001) face of α-Al_2O_3 in a neutral pH catalytic environment, was constructed using the CHARMM-GUI Nanomaterial Modeler input generator[41]. The lattice parameters of the orthorhombic unit cell contained cell lengths of a = 8.2 Å, b = 4.8 Å, and c = 13.0 Å, with 90° bond angles (α, β, γ)[41,42]. To model the surface, we employed the INTERFACE Force Field (IFF[42,43]), developed by Heinz et al. The resulting structure and topology files were converted from CHARMM to GROMACS format using the ParmEd[44] tool.

Surface hydroxyl groups were restrained from moving in the z-direction. This constraint aimed to maintain surface stability during the simulations (**Fig. S6**) and establish a fixed reference plane for determining the orthogonal distance between the polymer and surface during enhanced sampling with metadynamics (see section below). It also allowed for lateral molecular vibrational movement within the surface, consistent with the NPT ensemble.

Importantly, the inorganic-organic interface, formed by the metal oxide surface in the solid phase and solvated polymer in the liquid phase, utilized two different force fields: IFF and GAFF2, respectively. Compatibility between the two force fields was ensured by their equivalent definitions of non-bonded interactions. Both IFF and GAFF2 utilize the 12-6 Lennard-Jones potential and Lorentz-Berthelot mixing rule to describe van der Waals forces. Furthermore, the GAFF2 scaling factor for intramolecular 1-4 interactions was applied system-wide. This decision was made considering that IFF predominantly models the alumina surface as non-bonded, lacking specific Al-O bond potentials and thus 1-4 non-bonded interactions.

Metadynamics simulations

An important consideration for our model system is that typical hydrogenolysis catalysts consist of metal nanoparticles dispersed onto metal oxide supports[13] (e.g., ruthenium supported by alumina). As previously mentioned, we hypothesized that polymer adsorption thermodynamics are primarily governed by properties of the support and resulting polymer-support interactions. This assumption led us to simplify our system to focus solely on polymer-support interactions (**Fig. 1A**). Four systems were constructed, each comprising a single polyester oligomer initially positioned 1.8 nm (to prevent biases from short-range interaction effects) above the hydroxylated alumina surface measuring 5.8 x 5.7 x 2.8 nm^3 and surrounded by the solvent 1,4-dioxane. The substrate plane defining the interface is characterized by the horizontal plane measuring 5.8 x 5.7 nm^2. **Fig. 1B** provides a visualization example of initial system configuration and simulation box setup for the PET3 system. The box size was chosen to prevent self-interaction between periodic images in all three dimensions. PACKMOL[45] was employed to insert 1,676 solvent molecules into the 7.2 nm of free space above the alumina surface, corresponding to the experimental bulk density of 1,4-dioxide (1.033 g/cm^3) at 300 K. Since all structures used in the simulations were neutrally charged, there was no need to introduce counterions to maintain overall system charge neutrality. Detailed specifications of the four simulated systems are provided in **Table 1.**

Table 1. System setup of metadynamics simulations and representative chemical structures of polyester oligomers.

System	Polyester	Polyester End-to-End Dist. (nm)	No. of Atoms (Polyester)	No. of Atoms (System)
I	PLA5	1.8	48	35104
II	PET2	2.2	47	35103
III	PLA10	3.5	93	35149
IV	PET3	3.4	69	35125

PLA:

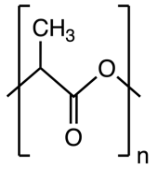

PLA5:

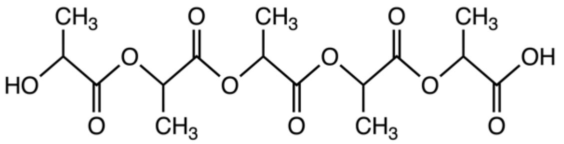

PLA10:

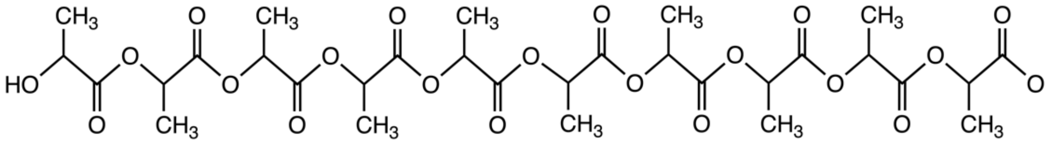

PET:

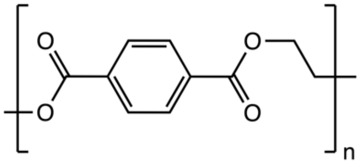

PET2:

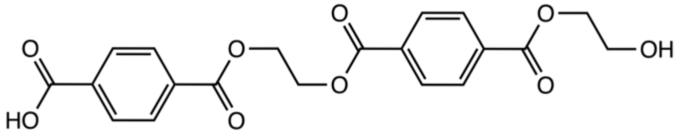

PET3:

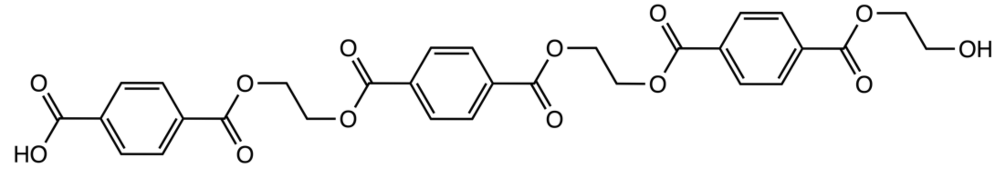

All simulations utilized the GROMACS 2021[46] MD simulation engine with the PLUMED 2.7.1[47] plugin. The simulation protocol consisted of several steps. First, a steepest descent energy minimization was performed on all systems. This was followed by a 2 ns NVT equilibration simulation, during which the temperature was maintained at 300 K using the Bussi-Donadio-Parrinello (velocity rescale) thermostat[48]. Subsequently, a 2 ns semi-isotropic NPT equilibration simulation was conducted at 300 K using the same thermostat and the Berendsen barostat[49] to equilibrate the pressure at 1 bar. Semi-isotropic coupling permitted expansion solely in the z-direction. Finally, semi-isotropic NPT production simulations were carried out at 300 K and 1 bar, employing the same thermostat and the Parrinello-Rahman barostat[50]. These latter simulations incorporated enhanced sampling techniques, as described below.

In all simulations, a timestep of 2 fs was used, achieved by constraining the bonds between hydrogen and other heavy atoms with the LINCS[51] algorithm. Long-range electrostatic interactions were computed via the particle mesh Ewald (PME[52]) summation method, employing a cutoff value of 1.2 nm. To truncate short-range Lennard-Jones interactions, a force switching scheme was applied, smoothly transitioning the force to zero between distances of 1.0 nm and the van der Waals cutoff of 1.2 nm. Additionally, all systems employed periodic boundary conditions (PBC) in the x, y, and z dimensions. To prevent undesired interactions between the polymer and the top periodic image of the surface, a "wall" potential was implemented using PLUMED in each system.

This potential acted solely on the polyester molecule and was activated when the distance between the polymer and the top of the simulation box was within 2 nm.

Building upon our previous research on peptide adsorption onto titania and silica surfaces[53], we utilized the well-tempered metadynamics (WTM[26]) enhanced sampling method. This approach enabled us to comprehensively explore the configurational space of the polyester oligomers and their interfacial interactions with the alumina surface, overcoming the timescale limitations of classical simulations. The σ values (Gaussian hill width) for the collective variables (CVs) in each system were calculated as half the equilibrium fluctuations of the respective CVs, leveraging trajectory data from the previously described 2 ns semi-isotropic, unbiased NPT equilibration simulation. Within this WTM sampling framework, we focused on two CVs: (1) the orthogonal distance between the alumina surface's top oxygen layer and the polyester's center-of-mass (Z), and (2) the radius of gyration of the polyester (Rg), as shown in **Fig. 1A**. The σ values for the Rg CV were determined to be 0.01 nm, 0.03 nm, 0.02 nm, and 0.025 nm for the PLA5, PLA10, PET2, and PET3 systems, respectively, with a value of 0.1 nm determined for the Z CV across all systems.

Metadynamics parameters, including the bias factor ($\gamma = 20$), bias deposition pace ($\tau = 1$ hills/ps), and initial hill height ($w_0 = 2.0$ kJ/mol), were held constant across all four WTM simulations. A grid with spacing independent of the Gaussian width, storing applied bias values, was implemented for each system to expedite the evaluation of the continuously growing number of Gaussian kernels as the WTM simulations progressed. As previously mentioned, a half harmonic restraint, or "wall" potential, was applied to the Z CV to confine sampling to one of the two mirrored surfaces resulting from PBC. Production WTM simulations were executed until convergence was achieved, defined as the point at which negligible changes over time were observed in the polyesters' Gibbs adsorption free energy differences (**Fig. S8**) and in the shapes of their reweighted free energy surfaces[27,54] projected onto both CVs (**Figs. S1-2**). A third metric used to evaluate convergence was a marked and sustained reduction in the height of the deposited Gaussian hills over time (**Fig. S4**). All systems demonstrated convergence after 1500 ns of production WTM simulation.

Simulation trajectory analysis

Trajectories from the production WTM simulations were visualized using Visual Molecular Dynamics (VMD[55]). The electron density profile (EDP) of the solvent was attained by extrapolating the atomic density distribution of solvent molecules above the surface to the theoretical bulk electron density. Free energy profiles and landscapes describing polyester adsorption to the alumina surface were constructed by reweighting for both system and wall biases applied during WTM simulations using the weighted histogram analysis method (WHAM[56]), implemented through PLUMED. This method resulted in reconstructed free energies proportional to the applied potential bias for each CV. Quantification of hydrogen bonding between alumina hydroxyl groups (hydrogen donors) and participating oligomer oxygens (hydrogen acceptors) of physisorbed polyesters was performed with a 3 Å donor-acceptor distance cutoff and 20° angle cutoff, using the HBonds plugin in VMD. We also conducted a 200 ns unbiased MD simulation of the PLA5 system to confirm the improved sampling efficiency across both CVs by applying WTM. In this comparison, we observed wider sampling ranges for the Rg CV and more frequent sampling of near-surface polyester states based on the Z CV in the WTM simulation **(Fig. S7**).

Configurational clustering was performed on all physically adsorbed polymer configurations sampled in each WTM simulation using the gromos[57] clustering method implemented in

GROMACS. Energetically accessible adsorbed polymer configurations were isolated based on criteria that included a polymer-surface orthogonal distance between 0.2 and 0.6 nm and being within 1.5 $k_B T$ of the adsorption free energy minimum. Root-mean-square deviation (RMSD) cutoff values of 0.2, 0.2, 0.3, and 0.25 nm were chosen for the PLA5, PET2, PLA10, and PET3 systems, respectively, to ensure a comparative cluster size distribution across the four systems based on their respective adsorbed configurations. According to the gromos clustering algorithm, the configuration with the largest number of neighbors, per the RMSD cutoff, is designated as the first cluster. Then, this configuration and its neighbors are considered successfully clustered and removed from the selection pool. This process iterates until each frame of the simulation trajectory that contains an adsorbed polymer configuration has been assigned to a cluster.

Results and Discussion

Surface chemistry effects on solvent layering

We selected the hydroxylated α-Al_2O_3 (0001) surface for MD simulations. The (0001) facet is a stable and widely observed facet of alumina, typically featuring a hydroxylated surface[61]. Alumina is characterized by its energetically stable corundum structure and finds widespread use as a substrate in the form of sapphire for high-resolution X-ray characterization of thin films and solid-liquid interfaces[61]. In addition to providing a model substrate relevant to supported alumina catalysts, use of this surface enables direct comparison to XRR experiments. Such a synergistic computational-experimental approach has previously proven successful with other model systems, including electrode-electrolyte interfaces for lithium-ion batteries[60]. For the simulated catalytic conditions under which the MD simulations were conducted, the top oxygen layer of alumina was fully hydroxylated (see Methods), consistent with the experimental sapphire substrates[60].

A representative snapshot illustrating the solvent layering behavior of 1,4-dioxane near the alumina surface, obtained from the final frame of the PLA5 WTM simulation, is shown in **Fig. 1D**. The normalized atom number density distribution of 1,4-dioxane as a function of distance from the alumina surface in the WTM simulations is depicted in **Fig. 1E**. Importantly, we expect the solvent atom number density distribution obtained from the WTM simulation to be unaffected by the application of enhanced sampling, as no biases were applied to the solvent molecules, and the lone polyester molecule is too small compared to the size of the simulation box to exert influence. To validate this, we compared the solvent atom number density profile from WTM to that calculated from the 200 ns unbiased PLA5 simulation and found strong agreement (**Fig. S5**).

We observed strong solvent layering above the alumina surface. This is captured in **Fig. 1E**, based on the respective atom number density peak contributions from the solvent molecules' centers-of-mass (COM) and characteristic atom groups (ether oxygens and methylene carbons). The first solvent layer consists of a bilayer with two adjacent peaks at 0.34 and 0.49 nm. These two partially overlapping solvent layers are not fully distinct from one another, resulting in an average layer spacing of ~0.45 nm. Subsequent solvent layers each consisted of a pair of distinctive high- and low-density regions centered around the bulk solvent density, with a spacing of ~0.47 nm. This type of layering behavior propagated through the sixth solvent layer, terminating at ~3 nm from the alumina surface. After this point, the surface's effects on solvent layering were not apparent as the amplitude of the corresponding mass distribution oscillation could not be distinguished. This phenomenon is consistent with the gradual decay of ordering at increasing distance away from the surface, as expected for solvents like 1,4-dioxane composed of relatively small molecules[60,62,63].

The orientational distribution of solvent molecules in the first layer was resolved by determining the contributions of the solvent molecules' COM, ether oxygen, and methylene carbon atoms. We found that the solvent's molecular plane preferentially aligns parallel to the surface with some degree of tilt. Analysis of the orientational distributions of near-surface solvent molecules indicated an average tilt angle of 55° formed between the vector along the solvent's molecular plane and the surface normal vector (**Fig. 1C**). On average, solvent molecules near the alumina surface preferentially orient more horizontally with respect to the surface. This deviation from a random orientational distribution highlights the influence of the alumina surface on interfacial solvent ordering. Observations of molecular plane reorientation among solvent molecules were further confirmed through visual analysis of the trajectories, where solvent molecules initially aligned parallel to the surface were observed to tilt and reorient themselves as the simulation progressed (**Fig. 1D** shows a representative snapshot from the simulations).

By extrapolating the atom number density distribution to the solvent's theoretical bulk electron density (0.34 $e^-/Å^3$), we derived the representative MD-derived EDP. The corresponding EDPs and normalized EDPs of the entire solvent molecule and its characteristic atom groups (ether oxygens and methylene carbons) are depicted in **Fig. S11** and **Fig. S12**, respectively. The solvent EDP offers another perspective on the surface layering behavior of 1,4-dioxane above alumina, which we utilized to initially connect our MD simulation to the experimental characterization of solid-liquid interfaces. Specifically, to predict the XRR scattering profile, we fit the MD-derived EDP data to the distorted crystal model (DCM; see SI Methods), which is applicable for describing molecular layering at solid surfaces. We achieved good agreement between the MD-derived EDP and the DCM fit-derived EDP upon optimizing DCM model parameters (**Fig. 1F**). The average spacing between layers was found to be 0.44 nm, consistent with the theoretical values previously discussed. Using the DCM fit values, we calculated the predicted structure factor, R/R_f (**Fig. 1G**), using **Eqns. S1-3**. A minimum observed at approximately 0.9 $Å^{-1}$ indicates variation in the EDP in the surface normal on the scale of $d = \pi/q_{min} = 0.35$ nm, consistent with the first molecular layer of 1,4-dioxane at the alumina interface observed in the simulations. These results permit direct comparison of our simulation results with initial data from XRR experiments, as illustrated in **Fig. S13**. This direct comparison of predicted XRR measurements from MD simulations to experimental data establishes a basis for future experimental tests of MD models in capturing solvent and polymer behaviors at catalyst surfaces and various other interfacial systems.

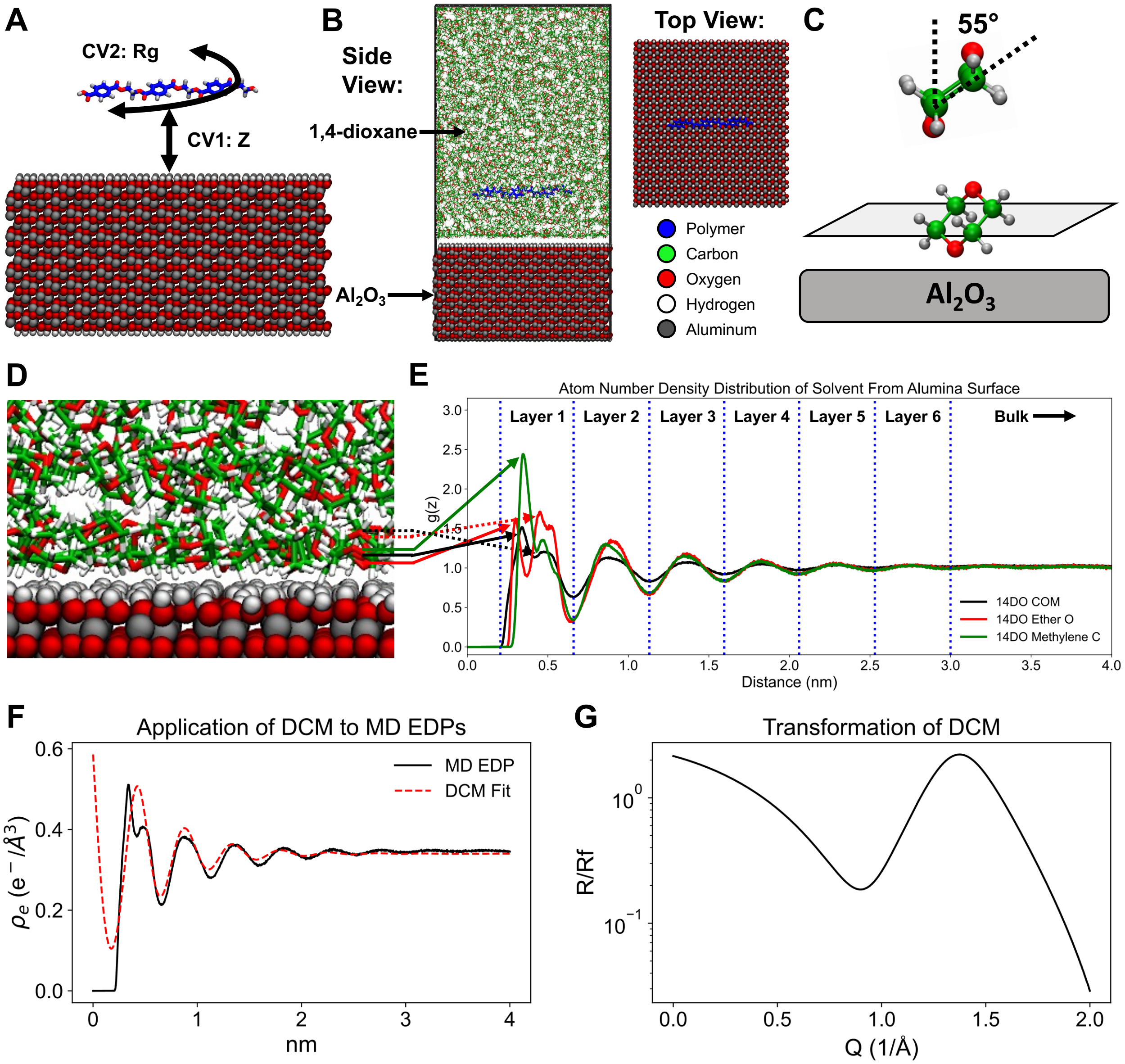

Figure 1. A) Depiction of polymer-surface orthogonal distance defined between the surface's top oxygen layer and polymer center-of-mass (COM; Z) and radius of gyration (Rg) WTM collective variables (CVs). B) Example initial system configuration and simulation box setup for WTM simulations, shown from both the side (left) and top (right) views. C) Illustration of the preferred tilt angle with respect to the surface normal vector (top) and near-surface configuration (bottom) of 1,4-dioxane molecules extracted from analysis of the molecular plane orientational distribution in WTM simulations. D) Representative snapshot of the final frame from WTM simulation (PLA5 system shown) illustrating 1,4-dioxane solvent layering behavior near the alumina surface. E) Normalized surface-orthogonal atom number density distribution of 1,4-dioxane above the alumina surface, labeled with layer cutoffs and first layer density peak assignments to its COM and characteristic atom groups (normalized to their respective bulk atomic density far from the interface); black: COM, red: ether oxygens, green: methylene carbons. F) Electron density profile (EDP) of 1,4-dioxane extrapolated from its atom number density distribution (solid black lines) and the corresponding EDP derived from fitting to the distorted crystal model (DCM; dashed red lines). G) Corresponding predicted structure factor (R/R_f) of X-ray reflectivity (XRR) obtained from fitting the MD-derived EDP to the DCM.

Polyester adsorption thermodynamics

Given the scarcity of available thermodynamic data on the physical adsorption of polyester oligomers and the challenges in obtaining atomic-scale insights through conventional experimental methods, we employed metadynamics-based enhanced sampling simulations to investigate these properties. By monitoring the evolution of Gibbs adsorption free energy differences between near-surface and bulk polyester states ($\Delta G_{ads-bulk}$), derived from reweighted trajectories using WHAM over consecutive 50 ns intervals, we identified simulation convergence as the point at which these values stabilized across all systems (**Fig. S8)**. Importantly, the adsorption free energy change of each polyester system eventually reached a plateau consistent with the values extracted from their respective adsorption free energy profiles (**Fig. 2D**), discussed below.

For ease of comparing adsorption free energy differences across the polyester oligomers, minima-adjusted adsorption free energy profiles (**Fig. 2D**) were obtained by vertically translating the unadjusted adsorption free energy profiles (**Fig. 2A**) such that the minima in the adsorbed region were set to zero for each system. Adsorption free energy differences were determined by subtracting the average free energy in the bulk region (3–4 nm) from that of the minima in the adsorbed region (~0.3–0.6 nm). We observed that PET oligomers adsorb much more strongly onto the alumina surface than PLA oligomers. Specifically, PET2 and PET3 exhibited adsorption free energies differences of -3.5 and -4.4 $k_B T$, respectively, compared to -1.4 and -1.1 $k_B T$ for PLA5 and PLA10. As noted earlier with regards to the convergence of the WTM simulations, the adsorption free energy differences among the four polyester oligomers are primarily influenced by the type of polyester and relatively independent of polyester chain length. For instance, despite PLA10 having a significantly longer chain length than PET2 (3.5 nm vs. 2.2 nm, respectively), it adsorbs less strongly to the surface with an adsorption free energy difference even lower than that of PLA5, which is more comparable in length to PET2 (1.8 nm vs. 2.2 nm). This result suggests that, at least within the length scale of oligomers we tested, the chemical effects of different polyester functional groups drive adsorption thermodynamics at the alumina surface.

Further analysis of the free energy profiles in **Fig. 2D** indicated a maximum in the adsorption free energies at orthogonal distances between 1 to 2 nm from the surface for all four polyesters (1.1, 1.3, 1.8, and 1.2 nm for PLA5, PET2, PLA10, and PET3, respectively). The highest free energy maxima observed for the PLA oligomers was approximately 2.4 $k_B T$, while for PET2, it was 5.5 $k_B T$, and for PET3, it was 6.1 $k_B T$. These free energy peaks are noticeably higher than the corresponding average free energy of each of the polyesters in the bulk region (3–4 nm), particularly for the PET oligomers. Thus, there exists a free energy barrier to adsorption as the polyesters approach the alumina surface, as well as to desorption upon polyester departure away from the alumina surface. This barrier is higher for PET oligomers (vs. the adsorbed and bulk free energies), but once overcome, it results in more favorable overall adsorption free energies compared to PLA oligomers. Moreover, the higher desorption barrier observed for PET oligomers suggests they are less likely to return to the bulk solution. This characteristic may result in a higher equilibrium coverage of surface-bound PET under steady state conditions, driven by free energy differences.

The existence of the free energy maxima can be attributed to the energetic penalty of the polyesters having to displace multiple solvent layers arranged in energetically favorable configurations above alumina, as discussed in the previous section. Solvent layering was observed up to 2.5–3.0 nm from the surface (**Fig. 1E**), corresponding to the approximate distance at which the free energy profiles of the polyesters begin to increase upon diffusion towards, and adsorption onto the alumina surface. Solvent displacement effects induced by oligomer adsorption were confirmed by subtle differences in the near-surface density distribution of solvent atoms extracted from portions of the simulation trajectory in which PET3 was either adsorbed versus in the bulk phase (**Fig. 2B**).

The height of the free energy barrier relative to the adsorption minimum is heavily dependent on the type of polyester, reinforcing the idea that polyester functional group chemistry dictates the overall adsorption thermodynamics at the polyester-alumina interface. Specifically, since the higher maximum observed for PET compared to PLA was largely independent of oligomer chain length, polyester functional group chemistry is hypothesized to be responsible for driving differences in the height of the free energy maxima. Interestingly, however, the free energy maxima of oligomers with longer chain lengths (PLA10, 3.5 nm; PET3, 3.4 nm) occurred at distances further from the surface. This result suggests that the onset of solvent layer displacement, or the point at which solvent displacement is complete and full desorption of the polyester into the bulk occurs, is more dependent on polyester chain length.

To gain additional insights into the above results, we examined the favorability of subsets of polyester configurations by analyzing configurational entropy differences between adsorbed and bulk states (see SI; **Eqn. S4**). Our calculations revealed an entropic penalty for the adsorption of larger polyesters (-1.9 and -2.6 J/mol·K for PLA10 and PET3, respectively), while the entropy difference upon surface adsorption of the smaller polyesters was found to be near-zero and positive (0.3 and 1.5 J/mol·K for PET2 and PLA5, respectively) (**Table S1**). Hence, the adsorption of polyesters with smaller chain lengths is more entropically favorable. This result demonstrates that the chain length of polyesters significantly impacts their adsorption entropy. It is therefore possible that the solvent displacement distance required for full desorption of larger polyesters is entropically driven by their unfavorable transition between different conformations on or near the surface. Additionally, this entropic effect may influence the adsorption free energy differences associated with these conformations discussed earlier.

Differences in the chemistry of polyester functional groups not only influence the adsorption free energy but also affect the preferred surface-separation distance of the adsorbed polyesters. For example, we observed that the PET oligomers preferentially adsorbed closer to the surface, with a COM distance of 0.37 nm for both PET oligomers, while the PLA oligomers preferred to adsorb slightly farther away from the surface at distances of 0.43 nm for PLA5 and 0.45 nm for PLA10 (**Fig. 2C**). This trend was confirmed by the atom number density distribution of the polyesters as a function of distance from the alumina surface in the WTM simulations (**Fig. S10**). Specifically, we found that the PET oligomers exhibited higher atomic densities in the first layer, with peaks located closer to the alumina surface compared to the PLA oligomers.

The preference of the PET oligomers for a closer surface-separation distance resulted in stronger interactions with the surface compared to the PLA oligomers. This is evidenced in **Fig. 2A**, which displays the non-minima-adjusted adsorption free energy profile for each system. In these plots, the free energies of the adsorbed-state minima reflect the binding strength between each polyester and the alumina surface, illustrating the PET oligomers' favorable surface interactions with free energies between -1 and -2 k_BT. In contrast, the PLA oligomers exhibited weaker interactions with the surface, with free energies between 0 and 1 k_BT. Moreover, we observed that PLA oligomers engaged in more favorable interactions with the solvent compared to PET oligomers, as indicated by their lower free energies in the bulk region. These findings indicate that the larger adsorption free energy differences of PET oligomers, as discussed earlier in **Figs. 2C-D**, stem from both their more favorable surface interactions and less favorable solvent interactions compared to PLA.

To further our understanding of the driving forces underlying the observed differences in polyester adsorption thermodynamics and behavior, we analyzed the preferred near-surface conformations of the polyesters by performing configurational clustering of the WTM simulation trajectories. **Figs. 2E-F** highlight the most energetically favorable polyester conformations obtained by clustering and reweighting free energy minima in the adsorbed (**Fig. 2E**) and bulk (**Fig. 2F**) regions, along with their respective cluster probabilities. We note that all top-clustered polyester configurations (see Methods) displayed higher cluster probabilities compared to their respective second-most probable clusters, confirming their dominance within the cluster ensemble. In the adsorbed region, only energetically accessible configurations were clustered, defined as those within 1.5 $k_B T$ of the free energy minimum. For the bulk region, all configurations within the range of 3-4 nm were clustered, as per previous analysis.

Additionally, we investigated the hydrogen bonding interactions between the alumina surface and various adsorbed polyester conformations, utilizing previously defined distance and angle cutoffs (see Methods). We quantified the number of hydrogen bonds formed between the surface hydroxyl groups of alumina and adsorbed polyester states. We then determined the time-averaged probabilities of hydrogen bond formation with alumina by hydrogen bond-accepting oxygens of each polyester oligomer observed throughout the simulations. Our analysis revealed probabilities of 2.5%, 2.9%, 1.6%, and 2.3% in hydrogen bond formation per oxygen for PLA5, PET2, PLA10, and PET3, respectively (**Fig. S9**). These findings indicate that PET oligomers' hydrogen bond-accepting oxygens can, on average, form more hydrogen bonds with surface hydroxyl groups than PLA at comparable oligomer length scales. Moreover, we observed that larger oligomers' hydrogen bond-accepting oxygens exhibited greater difficulty in forming hydrogen bonds with surface hydroxyl groups, most likely due to steric hindrance effects.

Our findings further indicate that the PET oligomers preferentially adopted a flattened conformation on alumina, facilitating the more uniform distribution of their atom groups at closer distances to the surface. Specifically, we observed that the PET oligomers' aromatic rings aligned parallel to the surface, an orientation unattainable for PLA methyl groups. These observations are consistent with our prior findings, wherein the adsorbed-state free energy well for the PET oligomers is closer to the surface (**Fig. 2C**), and a more concentrated density of PET atoms was found near the surface (**Fig. S10**), compared to the PLA oligomers. Interestingly, PLA oligomers adopted a more extended linear conformation upon adsorption, while PET oligomers adopted a more compact C-shaped configuration (**Fig. 2E**). Conversely, all four polyester oligomers were observed to favor an extended linear conformation in the bulk region (**Fig. 2F**), as expected given the absence of intermolecular interactions with the alumina surface and the drive to maximize overall system entropy. In summary, our investigation of interfacial polyester structures through configurational clustering provided a molecular basis crucially connecting polyester functional group chemistry to the observed trends in physisorption thermodynamics.

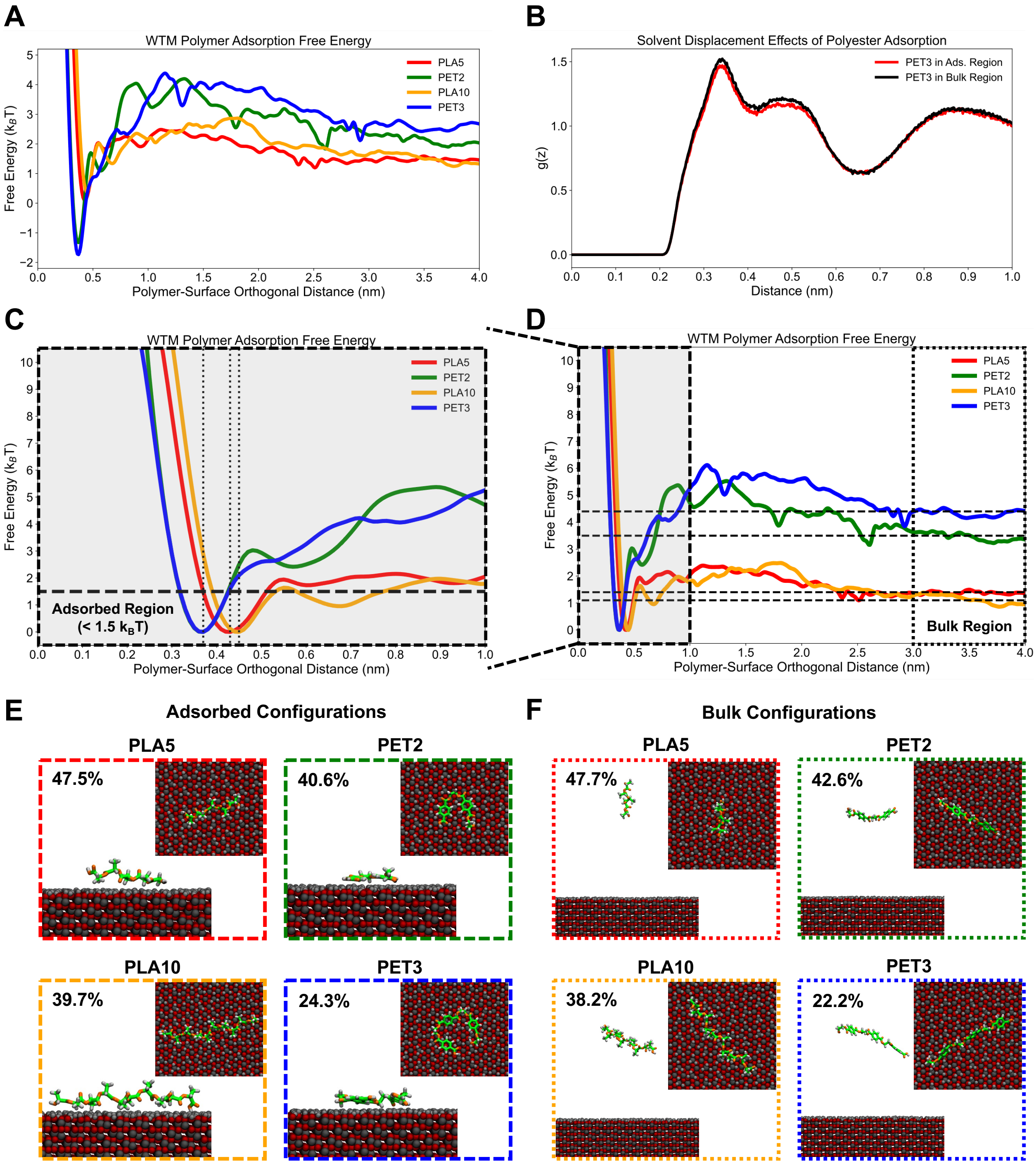

Figure 2. A) Full adsorption free energy profiles (no minima adjustment) along the Z CV featuring adsorption free energy minima and maxima for all polyesters (red: PLA5, green: PET2, orange: PLA10, blue: PET3). B) Normalized near-surface (less than 1 nm distance) solvent atom number distribution determined from simulation trajectory for when PET3 is physically adsorbed (red) and in bulk (black), demonstrating solvent displacement effects of polyester physisorption. C) Near-surface (less than 1 nm distance) adsorption free energy profiles along the Z CV, highlighting free energy minima for all polyesters (minima-adjusted to zero for each system; adsorbed region is defined as within 1.5 k_BT of the free energy minima). D) Full adsorption free energy profiles along the Z CV featuring free energy minima and maxima for all polyesters (minima-adjusted to zero for each system; bulk region is defined as between 3 and 4 nm in separation distance). E) Conformations of adsorbed polyester states with the highest probabilities from configurational clustering of the adsorbed region, along with corresponding cluster weights. F) Conformations of bulk

polyester states with the highest probabilities from configurational clustering of the bulk region, along with corresponding cluster weights.

Preferred conformations of surface-bound polyesters

In **Fig. 2**, polyester conformations were clustered based on 1D free energy profiles projected solely onto the Z CV. However, these conformations may not necessarily represent the most energetically favorable ones based on the second CV, Rg. Therefore, we characterized the 2D free energy profiles from the WTM simulations, projected onto both CVs simultaneously. Consistent with our previous findings, we observed broadly similar 2D free energy landscapes for the two PLA oligomers and two PET oligomers, as well as significant differences across polyester types (**Fig. 3A**). Specifically, larger free energy differences were again observed between the adsorbed and bulk regions for the PET oligomers compared to the PLA oligomers.

Upon examining the near-surface adsorption regions of the 2D free energy landscapes (**Fig. 3B**), we observed three and four distinct free energy minima for the smaller (PLA5 and PET2) and larger (PLA10 and PET3) polyester oligomers, respectively. For PLA oligomers, the adsorption free energy minima were located at Z values slightly above 0.4 nm, whereas those for PET oligomers were located slightly below 0.4 nm. This observation aligns with the location of free energy wells in the 1D free energy profiles and that of the first density peaks in the polyester atom number density distributions (**Fig. S10**) discussed earlier, from which we determined a smaller preferential surface-separation distance for PET oligomers compared to PLA oligomers.

Clustering and reweighting were then performed for each of the aforementioned free energy minima within their corresponding 2D phase space to elucidate the relationship between the preferred Rg and adsorbed-state conformations of each oligomer. As expected, the resulting most probable conformations, depicted in **Fig. 3C**, exhibited similar characteristics to those obtained from clustering the 1D adsorbed-state free energy minima based solely on the Z CV (**Fig. 2E**). However, our findings revealed multiple low free-energy conformations differing in Rg for each oligomer (**Fig. S3**), all contributing to the overall clustered adsorbed-state conformational ensemble associated with their respective 1D free energy profiles. Nonetheless, focusing on the lowest free energy conformations (labeled C1 for PLA5, PET2, and PLA10; and C3 for PET3), we found that PET oligomers preferentially adopted more compact structures closer to the surface, consistent with our earlier findings. Importantly, we refrained from directly comparing Rg values across the oligomers due to their differing chain lengths. For instance, while PLA5 appeared fully extended at a Rg of ~0.50-0.55 nm, PET2 exhibited full extension at a Rg of ~0.70 nm.

When comparing the clustered, lowest free energy adsorbed-state conformations for PET2 and PET3, we noted similarities in how consecutive monomer segments were oriented relative to one another above the surface. This led to the hypothesis of both an optimal distance and "hinge" angle between adsorbed, consecutive PET monomer segments, which may be a preferred spatial arrangement that minimizes the free energy, regardless of the overall PET chain length. We tested this hypothesis by calculating the COM separation distance and hinge angle between each pair of consecutive aromatic rings in PET2 (PET2-C1; **Fig. 3D**, left) and PET3 (PET3-C3; **Fig. 3D**, middle). We observed highly similar values between the aromatic rings in PET2 (129° and 0.96 nm, respectively) and one pair of rings in PET3 (136° and 0.98 nm), supporting the idea that PET segments adopt a consistent geometry upon adsorption. The second pair of aromatic rings in PET3 exhibited slightly lower values (106° and 0.87 nm), resulting in average PET values of 124° and 0.94 nm when adsorbed in the flattened C-shaped conformation. This suggests that the optimal distance and hinge angle between consecutive PET monomer segments are key factors in the stable adsorption of PET oligomers on the alumina surface.

Given the presence of flexible bonds between PET monomers, it was unsurprising that the second most favorable clustered adsorbed-state conformation for PET3 exhibited an S-shape (PET3-C3B; **Fig. 3D,** right). Notably, one pair of aromatic rings in the S-shaped PET3 shared nearly identical hinge angles and separation distances (106° and 0.86 nm) with those in the C-shaped PET3. However, we observed substantially reduced values for the second pair of rings in the S-shaped PET3 (89° and 0.77 nm). This finding suggests that surface-bound, S-shaped PET conformations may feature more sterically hindered aromatic ring arrangements compared to C-shaped PET conformations, resulting in them being slightly less energetically favorable.

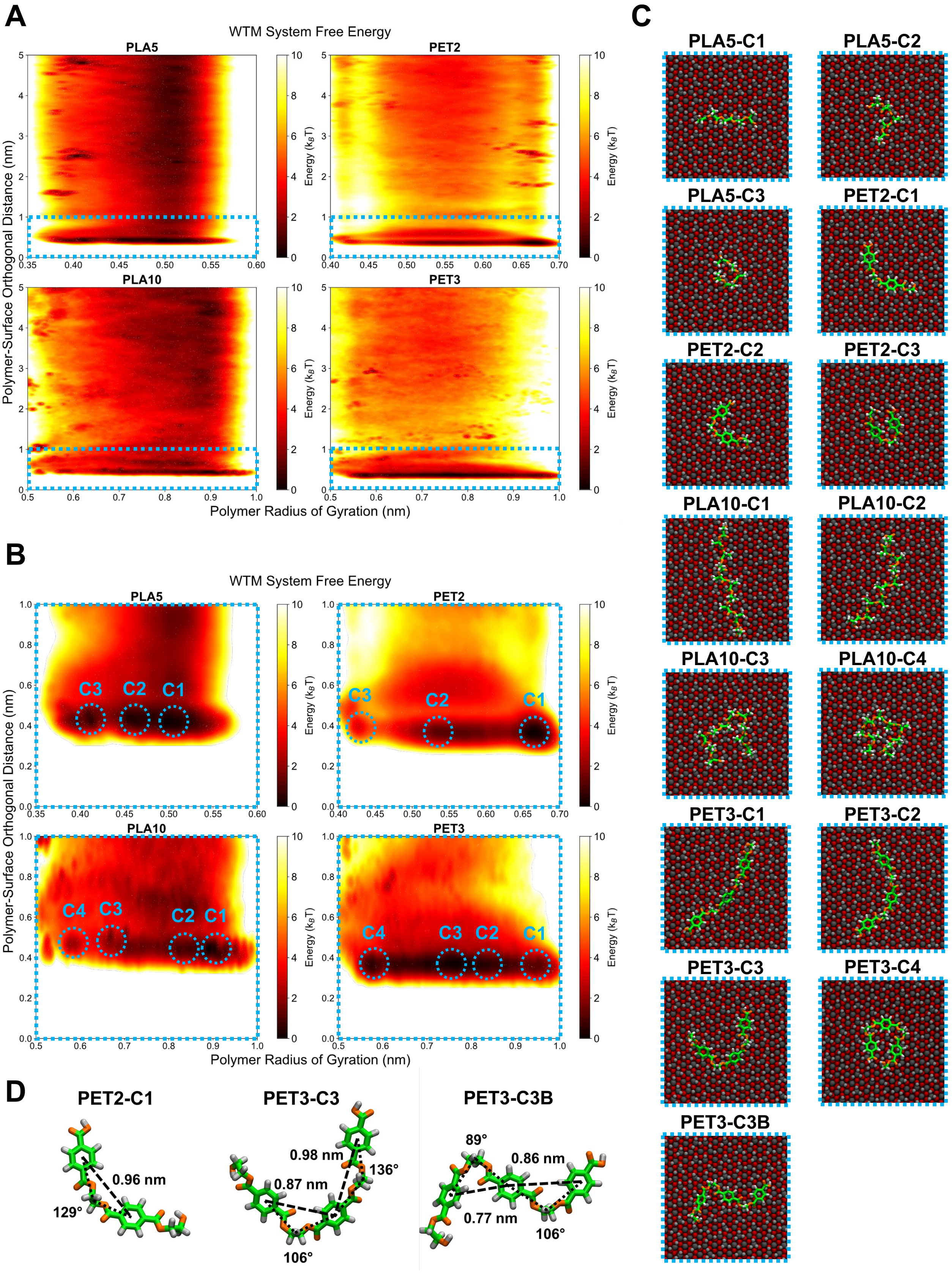
A
WTM System Free Energy
PLA5
PET2
PLA10
PET3
Polymer-Surface Orthogonal Distance (nm)
Polymer Radius of Gyration (nm)
Energy (k_BT)
0.35 0.40 0.45 0.50 0.55 0.60
0.40 0.45 0.50 0.55 0.60 0.65 0.70
0.5 0.6 0.7 0.8 0.9 1.0
0 1 2 3 4 5
0 2 4 6 8 10
B
WTM System Free Energy
PLA5
PET2
PLA10
PET3
C1
C2
C3
C4
Polymer-Surface Orthogonal Distance (nm)
Polymer Radius of Gyration (nm)
Energy (k_BT)
0.0 0.2 0.4 0.6 0.8 1.0
C
PLA5-C1
PLA5-C2
PLA5-C3
PET2-C1
PET2-C2
PET2-C3
PLA10-C1
PLA10-C2
PLA10-C3
PLA10-C4
PET3-C1
PET3-C2
PET3-C3
PET3-C4
PET3-C3B
D
PET2-C1
0.96 nm
129°
PET3-C3
0.98 nm
0.87 nm
136°
106°
PET3-C3B
89°
0.86 nm
0.77 nm
106°

Figure 3. A) 2D free energy profiles for each polyester depicting the complete free energy landscape of polyester-alumina interactions at their interface, constructed from FES reweighting analysis across both Z and Rg CVs using WHAM. B) Close-up examination of near-surface region (less than 1 nm in separation distance) within the 2D free energy profiles featuring multiple local free energy minima for each adsorbed polyester. C) Conformations of adsorbed polyester states (top view) with the highest probabilities from configurational clustering analysis of individual local free energy minima ('B' label for PET3 C3 configuration denotes second most probable clustered conformation). D) PET aromatic ring hinge angles and COM separation distances calculated for the free energy minima configurations of PET2 (C-shaped) and PET3 (C-shaped and S-shaped) demonstrating optimal adsorbed PET oligomer conformational geometry.

Molecular mechanisms of polyester adsorption

In this study, we examined the physisorption of polyester oligomers with varying functional group chemistry and chain length onto alumina, a common support material for supported-metal hydrogenolysis catalysts. Our findings revealed that the adsorption free energy differences of both polyester types were largely unaffected by chain length. Clustering analysis indicated that PET tend to adopt more flattened conformations closer to the surface, suggesting enhanced non-bonded interactions between PET monomer segments and the surface, contributing to overall favorable polymer-surface interactions. Conversely, steric hindrance prevented PLA methyl groups from simultaneously occupying close near-surface positions to maximize surface interactions.

Previous studies conducted by us[53,64] and others[21,31] showed that small-molecule adsorption onto silica is primarily driven by hydrogen bonding to surface silanol groups, as well as the degree of protonation of these groups under different pH conditions. Hence, we posited differential hydrogen bonding to be the dominant type of non-bonded interaction driving the observed differences in adsorption strength between PLA and PET in our current study. The ability of these polyesters to act as hydrogen bond acceptors through their carbonyl and ether oxygens, combined with the ability of alumina hydroxyl groups to act as hydrogen bond donors, influences the polyesters' overall propensity to form hydrogen bonds with the surface, affecting their adsorption strength.

Hydrogen bonding analysis confirmed the higher propensity of PET to form hydrogen bonds with the alumina surface compared to PLA. Specifically, it was revealed that the hydrogen bond-accepting oxygens of PET oligomers were more likely to form hydrogen bonds with the surface hydroxyl groups of alumina than those of PLA oligomers (**Fig. S9**). This was observed across all energetically accessible states in the polyesters' respective adsorbed regions. Not surprisingly, the probability of hydrogen bond formation with alumina was reduced for larger oligomers (PLA10, PET3), likely due to greater steric challenges of all polyester oxygens forming hydrogen bonds with the surface simultaneously. As PET oligomers were found to adsorb closer to the alumina surface, they then have a higher propensity to form hydrogen bonds with the surface, despite having fewer available hydrogen bond-accepting oxygens compared to PLA oligomers. Clustering analysis suggested other aspects of alumina surface chemistry may also have facilitated the flattened conformations of PET oligomers, enabling them to associate closer to the surface than PLA oligomers. This was evidenced by the finding that PET aromatic groups consistently aligned parallel to the surface when physically adsorbed, unlike in the bulk.

Besides polymer-surface interactions, polymer-solvent interactions are also influential in driving the stronger adsorption observed for PET compared to PLA oligomers on the alumina surface. Our findings revealed that PET oligomers faced higher free energy barriers during their approach to and departure from the alumina surface. Since adsorption at a solid-liquid interface involves an activation process linked to the solvent-surface binding free energy[65,66], we attributed this free energy barrier to solvent layer displacement. This assertion was supported by near-surface solvent density analysis and free energy calculations, which showed that PET oligomers interacted less favorably with the solvent (1,4-dioxane) upon adsorption compared to PLA oligomers, contributing to higher PET adsorption free energy differences. Consequently, we propose that the aromatic ring groups of PET, due to their larger size and less favorable interactions with solvent molecules compared to the methyl groups of PLA, encountered greater challenges in displacing solvent layers above the alumina surface. Additionally, PET oligomers preferred to adopt non-linear conformations upon adsorption, necessitating greater disruption of the stable arrangements of solvent ether oxygens present at the interface. Collectively, our results suggest that PET's more favorable interactions with the surface and less favorable interactions with the solvent compared to PLA both contributed to its higher adsorption free energy differences.

To characterize the optimal conformational geometry of physisorbed PET oligomers, we calculated the center-of-mass separation distance and the "hinge" angle formed between consecutive aromatic ring groups in the lowest free energy conformations of the PET oligomers. These optimal separation distances and angles can be utilized to predict a threshold chain length at which the oligomer would overlap end-to-end, rendering the C-shaped conformation less favorable due to steric hindrance. By extrapolating from the identified optimal values, we determined that this threshold corresponds to an oligomer chain length of six PET monomer units. Clustering analysis suggests that beyond this threshold size, the next most probable and likely prevalent adsorbed PET oligomer conformation is S-shaped. However, past studies indicate that with further increases in chain length, it will eventually become energetically unfavorable for the entire chain to remain adsorbed to the surface. Instead, we would expect to observe only a fraction of the polymer chain adsorbed onto the surface, while the remaining portions reside non-adsorbed in the bulk[21].

Considering that physical adsorption and desorption represent only the initial and final steps, respectively, of adsorbate-surface interactions at a solid-liquid interface, understanding the adsorbate's behavior post-binding is crucial. In supported-metal catalysts, the strength of adsorbate-support interactions can significantly impact lateral diffusion of the adsorbate towards the catalytic junction at the metal-support interface. Notably, these lateral diffusion processes occur on much shorter timescales than surface adsorption or desorption[21]. With strong surface-adsorbate interactions, adsorbates can "crawl" on the surface, achieving lateral mobility without desorption[22,67], while moderately strong interactions may prompt repeated desorption into the bulk and readsorption, with readsorption probabilities governed by the sticking coefficient[23]. This interaction strength thus determines whether the adsorbate will return fully to the bulk phase or remain adsorbed upon making repeated, rapid bulk excursions, illustrating alternative routes for adsorbates to achieve surface lateral displacement within the timescale of such excursions. These phenomena are captured as "hopping" events, leading to "flight" motions for the adsorbate if its readsorption rate dominates the desorption rate[21,24].

The stronger observed adsorption of PET onto alumina suggests that PET may encounter greater challenges in diffusing laterally towards the active metal nanoparticles once attached to the support surface. PET's closer proximity to the surface and its preference for more compact conformations upon adsorption also indicate reduced mobility on the surface, potentially hindering its transport towards active metal nanoparticles in supported catalysts. These results may provide a possible molecular-level explanation contributing to the higher temperature reaction conditions necessary to depolymerize PET compared to PLA observed in experiments[5], as elevated temperature would provide additional kinetic energy for PET to overcome strong surface binding forces and facilitate lateral diffusion. However, it is essential to note that other factors may also play a role. Thus, in designing supported-metal catalysts for mixed stream polyester hydrogenolysis, it is imperative to consider strategies for controlling the balance of adsorption and desorption strength between the polymer and support surface. Such strategies may involve chemical surface modification and precise tuning of solvent properties[24].

Considering the complexities surrounding the surface lateral diffusion of polymers, future simulations of this behavior will likely require enhanced sampling techniques, as employed in the current study. Collective variables based on lateral polymer coordinates and/or the number of polymer-surface hydrogen bonds could be utilized to fully explore the surface diffusion behavior of single polymer molecules. Furthermore, parallel tempering (temperature replica exchange) metadynamics simulations can leverage temperature effects to achieve highly efficient sampling of lateral, surface-bound polymer movements[53,68–72]. Ultimately, simulations using these enhanced sampling techniques will enable highly accurate predictions of polymer lateral diffusion behavior. This, in turn, can lead to the design of more effective catalysts that operate under optimized conditions, thereby improving the efficiency of hydrogenolysis reactions. Rigorous future analyses, including studies of adsorption residence times and distributions of lateral positions across adsorbed polymer states, will provide a better understanding of the thermodynamic driving forces and timescales underlying surface lateral diffusion of short, adsorbed polymer oligomers. Such understanding can significantly advance catalytic processes like hydrogenolysis by enabling more precise control over reaction conditions, thus paving the way toward a circular plastics economy and contributing to a sustainable, carbon-neutral energy infrastructure.

Conclusions

In summary, our results suggest key implications for optimizing hydrogenolysis by simultaneously adjusting three parameters related to polymer physisorption thermodynamics. Firstly, the adsorption free energy difference between the adsorbed and desorbed states of the polymer is crucial. The difference should be substantial enough to strongly favor the adsorbed state over the desorbed state. Ideally, this free energy difference should primarily result from tuning polymer-solvent interactions to be relatively weak rather than tuning polymer-support interactions to be relatively strong, for reasons provided next. Secondly, the absolute free energy of the adsorbed state can be controlled by adjusting the strength of polymer-support interactions. If these interactions are too strong, they may hinder surface lateral diffusion of the polymer towards the catalytic junction once adsorbed. Lastly, the free energy barrier to adsorption and desorption plays a critical role that must be considered. While a higher barrier may be effective at keeping the polymer on the surface, it may also impede adsorption unless the reaction temperature is sufficiently high to overcome this barrier. Ideally, there should be minimal-to-no free energy barrier to adsorption and desorption, which can be achieved by controlling solvent-support interactions. At the same time, a significant adsorption free energy difference must still be maintained to prevent polymer desorption. In all, these principles can serve as design rules to guide improved catalytic designs for hydrogenolysis, ultimately advancing towards a circular plastics economy. However, future work should also consider how these design rules might differ for scenarios involving mixed polymer streams.

Supporting Information

- Supplemental Methods: X-ray reflectivity experimental procedure, application of distorted crystal model (DCM), calculation of configurational entropy differences between adsorbed and bulk polyester states.
- Supplemental Results: Stability of non-bonded alumina model, WTM simulation convergence, configurational entropies of polyester states.
- Supplemental Figures: Evolution of 1D free energy profiles for collective variables (CVs) Z and Rg, complete 1D free energy profiles for collective variable Rg, evolution of deposited Gaussian hill biases during WTM simulations, comparison of solvent atom number density distribution between unbiased and WTM simulations, system and alumina surface root mean square deviation (RMSD) analysis, comparison of sampled CV ranges between unbiased and WTM simulations, evolution of Gibbs free energy differences between adsorbed and bulk polyester states, time-averaged probabilities of hydrogen bond formation between alumina and polyesters, atomic density distribution of polyesters sampled above alumina surface, solvent electron density profiles (EDPs), comparison of predicted structure factor (R/R_f) for the solvent-alumina interface from MD simulation to experimental X-ray reflectivity (XRR) data.

Acknowledgements

This work was funded by the NSF EFRI E3P award (2132033). This work also utilized resources from the University of Colorado Boulder Research Computing Group, which is supported by the National Science Foundation (awards ACI-1532235 and ACI-1532236), the University of Colorado Boulder, and Colorado State University. We thank Daniel K. Schwartz and Michael R. Shirts for their insightful contributions to the discussion of this work.

Z. D. and K. G. S. conceptualization;
Z. D. and E. E. D. formal analysis;
J. W. M., M. F. T. and K. G. S. funding acquisition;
Z. D., E. E. D. and A. B. W. investigation;
Z. D., E. E. D. and K. G. S. methodology;
J. W. M., M. F. T. and K. G. S. supervision;
Z. D. and E. E. D. writing – original draft;
Z. D., E. E. D., J. W. M., M. F. T. and K. G. S. writing – review and editing;

References

1. Jehanno, C. *et al.* Critical advances and future opportunities in upcycling commodity polymers. *Nature* **603**, 803–814 (2022).
2. Lange, J.-P. Managing Plastic Waste─Sorting, Recycling, Disposal, and Product Redesign. *ACS Sustain Chem Eng* **9**, 15722–15738 (2021).
3. Ellis, L. D. *et al.* Chemical and biological catalysis for plastics recycling and upcycling. *Nat Catal* **4**, 539–556 (2021).

4. Hou, Q. *et al.* Upcycling and catalytic degradation of plastic wastes. *Cell Rep Phys Sci* **2**, 100514 (2021).
5. Westhues, S., Idel, J. & Klankermayer, J. Molecular catalyst systems as key enablers for tailored polyesters and polycarbonate recycling concepts. *Sci Adv* **4**, 9669 (2018).
6. Celik, G. *et al.* Upcycling Single-Use Polyethylene into High-Quality Liquid Products. *ACS Cent Sci* **5**, 1795–1803 (2019).
7. Kots, P. A. *et al.* Polypropylene Plastic Waste Conversion to Lubricants over Ru/TiO2 Catalysts. *ACS Catal* **11**, 8104–8115 (2021).
8. Kots, P. A., Vance, B. C. & Vlachos, D. G. Polyolefin plastic waste hydroconversion to fuels, lubricants, and waxes: a comparative study. *React Chem Eng* **7**, 41–54 (2022).
9. Hibbitts, D. D., Flaherty, D. W. & Iglesia, E. Effects of Chain Length on the Mechanism and Rates of Metal-Catalyzed Hydrogenolysis of n-Alkanes. *J Phys Chem C* **120**, 8125–8138 (2016).
10. Rorrer, J. E., Beckham, G. T. & Román-Leshkov, Y. Conversion of Polyolefin Waste to Liquid Alkanes with Ru-Based Catalysts under Mild Conditions. *JACS Au* **1**, 8–12 (2021).
11. Rorrer, J. E., Troyano-Valls, C., Beckham, G. T. & Román-Leshkov, Y. Hydrogenolysis of Polypropylene and Mixed Polyolefin Plastic Waste over Ru/C to Produce Liquid Alkanes. *ACS Sustain Chem Eng* **9**, 11661–11666 (2021).
12. Rorrer, J. E. *et al.* Role of Bifunctional Ru/Acid Catalysts in the Selective Hydrocracking of Polyethylene and Polypropylene Waste to Liquid Hydrocarbons. *ACS Catal* **12**, 13969–13979 (2022).
13. Liu, L. & Corma, A. Metal Catalysts for Heterogeneous Catalysis: From Single Atoms to Nanoclusters and Nanoparticles. *Chem Rev* **118**, 4981–5079 (2018).
14. Augustine, R. L. *Heterogeneous Catalysis for the Synthetic Chemist*. (CRC Press, 1995). doi:10.1201/9781003067122.
15. Li, Y., Zhang, Y., Qian, K. & Huang, W. Metal–Support Interactions in Metal/Oxide Catalysts and Oxide–Metal Interactions in Oxide/Metal Inverse Catalysts. *ACS Catal* **12**, 1268–1287 (2022).
16. Liu, L. & Corma, A. Metal Catalysts for Heterogeneous Catalysis: From Single Atoms to Nanoclusters and Nanoparticles. *Chem Rev* **118**, 4981–5079 (2018).
17. Jenkins, A. H., Dunphy, E. E., Toney, M. F., Musgrave, C. B. & Medlin, J. W. Tailoring the Near-Surface Environment of Rh Single-Atom Catalysts for Selective CO2 Hydrogenation. *ACS Catal* **13**, 15340–15350 (2023).
18. Jenkins, A. H. & Medlin, J. W. Controlling Heterogeneous Catalysis with Organic Monolayers on Metal Oxides. *Acc Chem Res* **54**, 4080–4090 (2021).
19. Rorrer, J. E. *et al.* Role of Bifunctional Ru/Acid Catalysts in the Selective Hydrocracking of Polyethylene and Polypropylene Waste to Liquid Hydrocarbons. *ACS Catal* **12**, 13969–13979 (2022).
20. Klaimy, S. *et al.* Flash Catalytic Pyrolysis of Polyethylene over (Alumino)silicate Materials. *ChemCatChem* **12**, 1109–1116 (2020).
21. Yu, C., Guan, J., Chen, K., Bae, S. C. & Granick, S. Single-Molecule Observation of Long Jumps in Polymer Adsorption. *ACS Nano* **7**, 9735–9742 (2013).
22. Wong, J. S. S., Hong, L., Bae, S. C. & Granick, S. Polymer Surface Diffusion in the Dilute Limit. *Macromolecules* **44**, 3073–3076 (2011).

23. Skaug, M. J., Mabry, J. & Schwartz, D. K. Intermittent Molecular Hopping at the Solid-Liquid Interface. *Phys Rev Lett* **110**, 256101 (2013).
24. Wang, D. & Schwartz, D. K. Non-Brownian Interfacial Diffusion: Flying, Hopping, and Crawling. *J Phys Chem C* **124**, 19880–19891 (2020).
25. Laio, A., Parrinello, M. & Chandler, D. Escaping free-energy minima. *PNAS* **99**, 12562–12566 (2002).
26. Barducci, A., Bussi, G. & Parrinello, M. Well-tempered metadynamics: A smoothly converging and tunable free-energy method. *Phys Rev Lett* **100**, 1–4 (2008).
27. Barducci, A., Bonomi, M. & Parrinello, M. Metadynamics. *Wiley Interdiscip Rev Comput Mol Sci* **1**, 826–843 (2011).
28. Angioletti-Uberti, S., Ceriotti, M., Lee, P. D. & Finnis, M. W. Solid-liquid interface free energy through metadynamics simulations. *Phys Rev B* **81**, 125416 (2010).
29. Bačová, P. *et al.* Coupling between Polymer Conformations and Dynamics Near Amorphous Silica Surfaces: A Direct Insight from Atomistic Simulations. *Nanomaterials* **11**, 2075 (2021).
30. Cho, S., Jeong, S., Kim, J. M. & Baig, C. Molecular dynamics for linear polymer melts in bulk and confined systems under shear flow. *Sci Rep* **7**, 9004 (2017).
31. Perrin, E., Schoen, M., Coudert, F.-X. & Boutin, A. Structure and Dynamics of Solvated Polymers near a Silica Surface: On the Different Roles Played by Solvent. *J Phys Chem B* **122**, 4573–4582 (2018).
32. Tong, Z., Xie, Y. & Zhang, Y. Molecular dynamics simulation on the interaction between polymer inhibitors and β-dicalcium silicate surface. *J Mol Liq* **259**, 65–75 (2018).
33. Taib, N.-A. A. B. *et al.* A review on poly lactic acid (PLA) as a biodegradable polymer. *Polym Bull* **80**, 1179–1213 (2023).
34. Hanwell, M. D. *et al.* Avogadro: an advanced semantic chemical editor, visualization, and analysis platform. *J Cheminform* **4**, 17 (2012).
35. Frisch, M. J. *et al.* Gaussian 16 Revision C.01. Preprint at (2016).
36. Wang, J., Wang, W., Kollman, P. A. & Case, D. A. Automatic atom type and bond type perception in molecular mechanical calculations. *J Mol Graph Model* **25**, 247–260 (2006).
37. Bayly, C. I., Cieplak, P., Cornell, W. & Kollman, P. A. A well-behaved electrostatic potential based method using charge restraints for deriving atomic charges: the RESP model. *J Phys Chem* **97**, 10269–10280 (1993).
38. Case, D. A. *et al.* The Amber biomolecular simulation programs. *J Comput Chem* **26**, 1668–1688 (2005).
39. Wang, J., Wolf, R. M., Caldwell, J. W., Kollman, P. A. & Case, D. A. Development and testing of a general Amber force field. *J Comput Chem* **25**, 1157–1174 (2004).
40. Sousa Da Silva, A. W. & Vranken, W. F. ACPYPE - AnteChamber PYthon Parser interfacE. *BMC Res Notes* **5**, 367 (2012).
41. Choi, Y. K. *et al.* CHARMM-GUI Nanomaterial Modeler for Modeling and Simulation of Nanomaterial Systems. *J Chem Theory Comput* **18**, 479–493 (2022).
42. Kanhaiya, K. *et al.* Accurate Force Fields for Atomistic Simulations of Oxides, Hydroxides, and Organic Hybrid Materials up to the Micrometer Scale. *J Chem Theory Comput* **19**, 8293–8322 (2023).

43. Heinz, H., Lin, T.-J., Kishore Mishra, R. & Emami, F. S. Thermodynamically Consistent Force Fields for the Assembly of Inorganic, Organic, and Biological Nanostructures: The INTERFACE Force Field. *Langmuir* **29**, 1754–1765 (2013).
44. Shirts, M. R. *et al.* Lessons learned from comparing molecular dynamics engines on the SAMPL5 dataset. *J Comput Aided Mol Des* **31**, 147–161 (2017).
45. Martínez, L., Andrade, R., Birgin, E. G. & Martínez, J. M. PACKMOL: A package for building initial configurations for molecular dynamics simulations. *J Comput Chem* **30**, 2157–2164 (2009).
46. Abraham, M. J. *et al.* GROMACS: High performance molecular simulations through multi-level parallelism from laptops to supercomputers. *SoftwareX* **1–2**, 19–25 (2015).
47. Tribello, G. A., Bonomi, M., Branduardi, D., Camilloni, C. & Bussi, G. PLUMED 2: New feathers for an old bird. *Comput Phys Commun* **185**, 604–613 (2014).
48. Bussi, G., Donadio, D. & Parrinello, M. Canonical sampling through velocity rescaling. *J Chem Phys* **126**, 014101 (2007).
49. Berendsen, H. J. C., Postma, J. P. M., van Gunsteren, W. F., DiNola, A. & Haak, J. R. Molecular dynamics with coupling to an external bath. *J Chem Phys* **81**, 3684–3690 (1984).
50. Parrinello, M. & Rahman, A. Polymorphic transitions in single crystals: A new molecular dynamics method. *J Appl Phys* **52**, 7182–7190 (1981).
51. Hess, B., Bekker, H., Berendsen, H. J. C. & Fraaije, J. G. E. M. LINCS: A linear constraint solver for molecular simulations. *J Comput Chem* **18**, 1463–1472 (1997).
52. Darden, T., York, D. & Pedersen, L. Particle mesh Ewald: An N·log(N) method for Ewald sums in large systems. *J Chem Phys* **98**, 10089–10092 (1993).
53. Mao, C. M., Sampath, J., Sprenger, K. G., Drobny, G. & Pfaendtner, J. Molecular Driving Forces in Peptide Adsorption to Metal Oxide Surfaces. *Langmuir* **35**, 5911–5920 (2019).
54. Tiwary, P. & Parrinello, M. A Time-Independent Free Energy Estimator for Metadynamics. *J Phys Chem B* **119**, 736–742 (2015).
55. Humphrey, W., Dalke, A. & Schulten, K. VMD: Visual molecular dynamics. *J Mol Graph* **14**, 33–38 (1996).
56. Bonomi, M., Barducci, A. & Parrinello, M. Reconstructing the equilibrium Boltzmann distribution from well-tempered metadynamics. *J Comput Chem* **30**, 1615–1621 (2009).
57. Daura, X., Gademann, K., Jaun, B., van Gunsteren, W. F. & Mark, A. E. Peptide Folding: When Simulation Meets Experiment. *Angew Chem Int Ed* **38**, 236–240 (2004).
58. Mezger, M. *et al.* Molecular Layering of Fluorinated Ionic Liquids at a Charged Sapphire (0001) Surface. *Science (1979)* **322**, 424–428 (2008).
59. Cao, C., Steinrück, H.-G., Shyam, B., Stone, K. H. & Toney, M. F. In Situ Study of Silicon Electrode Lithiation with X-ray Reflectivity. *Nano Lett* **16**, 7394–7401 (2016).
60. Steinrück, H.-G. *et al.* The nanoscale structure of the electrolyte–metal oxide interface. *Energy Environ Sci* **11**, 594–602 (2018).
61. Fu, Q., Wagner, T. & Rühle, M. Hydroxylated α-Al2O3 (0001) surfaces and metal/α-Al2O3 (0001) interfaces. *Surf Sci* **600**, 4870–4877 (2006).

62. Xue, L., Keblinski, P., Phillpot, S. R., Choi, S. U.-S. & Eastman, J. A. Effect of liquid layering at the liquid–solid interface on thermal transport. *Int J Heat Mass Transf* **47**, 4277–4284 (2004).
63. Patil, U. & Caffrey, N. M. The role of solvent interfacial structural ordering in maintaining stable graphene dispersions. *2d Mater* **11**, 015017 (2024).
64. Sprenger, K. G., Prakash, A., Drobny, G. & Pfaendtner, J. Investigating the Role of Phosphorylation in the Binding of Silaffin Peptide R5 to Silica with Molecular Dynamics Simulations. *Langmuir* **34**, 1199–1207 (2018).
65. Honciuc, A., Howard, A. L. & Schwartz, D. K. Single Molecule Observations of Fatty Acid Adsorption at the Silica/Water Interface: Activation Energy of Attachment. *The J Phys Chem C* **113**, 2078–2081 (2009).
66. Honciuc, A., Baptiste, D. Jn., Campbell, I. P. & Schwartz, D. K. Solvent Dependence of the Activation Energy of Attachment Determined by Single Molecule Observations of Surfactant Adsorption. *Langmuir* **25**, 7389–7392 (2009).
67. Desai, T. G., Keblinski, P., Kumar, S. K. & Granick, S. Modeling Diffusion of Adsorbed Polymer with Explicit Solvent. *Phys Rev Lett* **98**, 218301 (2007).
68. Sugita, Y. & Okamoto, Y. Replica-exchange molecular dynamics method for protein folding. *Chem Phys Lett* **314**, 141–151 (1999).
69. Laio, A. & Gervasio, F. L. Metadynamics: a method to simulate rare events and reconstruct the free energy in biophysics, chemistry and material science. *Rep Prog Phys* **71**, 126601 (2008).
70. Bussi, G., Gervasio, F. L., Laio, A. & Parrinello, M. Free-Energy Landscape for β Hairpin Folding from Combined Parallel Tempering and Metadynamics. *J Am Chem Soc* **128**, 13435–13441 (2006).
71. Deighan, M., Bonomi, M. & Pfaendtner, J. Efficient Simulation of Explicitly Solvated Proteins in the Well-Tempered Ensemble. *J Chem Theory Comput* **8**, 2189–2192 (2012).
72. Sprenger, K. G. & Pfaendtner, J. Strong Electrostatic Interactions Lead to Entropically Favorable Binding of Peptides to Charged Surfaces. *Langmuir* **32**, 5690–5701 (2016).